

The X-ray coronae of the two brightest galaxies in the Coma cluster

J. S. Sanders¹, A. C. Fabian², M. Sun³, E. Churazov^{4,5}, A. Simionescu^{6,7,8},
 S. A. Walker² and N. Werner^{6,7}

¹ Max-Planck-Institut für extraterrestrische Physik, Giessenbachstrasse 1, 85748 Garching, Germany

² Institute of Astronomy, Madingley Road, Cambridge, CB3 0HA

³ Department of Physics, University of Alabama in Huntsville, Huntsville, AL 35899, USA

⁴ Max-Planck-Institut für Astrophysik, Karl-Schwarzschild-Strasse 1, 85748 Garching, Germany

⁵ Space Research Institute (IKI), Profsoyuznaya 84/32, Moscow 117997, Russia

⁶ KIPAC, Stanford University, 452 Lomita Mall, Stanford, CA 94305, USA

⁷ Department of Physics, Stanford University, 382 Via Pueblo Mall, Stanford, CA 94305-4060, USA

⁸ Institute of Space and Astronautical Science (ISAS), JAXA, 3-1-1 Yoshinodai, Chuo-ku, Sagamihara, Kanagawa 252-5210, Japan

20 September 2018

ABSTRACT

We use deep *Chandra* X-ray Observatory observations to examine the coronae of the two brightest cluster galaxies in the Coma cluster of galaxies, NGC 4874 and NGC 4889. We find that NGC 4889 hosts a central depression in X-ray surface brightness consistent with a cavity or pair of cavities of radius 0.6 kpc. If the central cavity is associated with an AGN outburst and contains relativistic material, its enthalpy should be around 5×10^{55} erg. The implied heating power of this cavity would be around an order of magnitude larger than the energy lost by X-ray emission. It would be the smallest and youngest known cavity in a brightest cluster galaxy and the lack of over pressuring implies heating is still gentle. In contrast, NGC 4874 does not show any evidence for cavities, although it hosts a well-known wide-angle-tail radio source which is visible outside the region occupied by the X-ray corona. These two galaxies show that AGN feedback can behave in varied ways in the same cluster environment.

Key words: galaxies: ISM — X-rays: galaxies — X-rays: galaxies: clusters

1 INTRODUCTION

Contrary to theoretical expectations, it was found that the two dominant central galaxies in the Coma cluster, NGC 4874 and NGC 4889, showed extended X-ray emission from their interstellar medium (Vikhlinin et al. 2001). This material was found to be confined by the pressure of the surrounding intracluster medium (ICM). Sun et al. (2007) examined a sample of galaxies in clusters, finding these embedded coronae to be relatively common (> 60% in galaxies with $L_{K_s} > 2L_*$), but with decreasing likelihood in hotter environments. Although these galactic coronae are smaller than those found outside groups and clusters, their high abundance shows that they are able to survive for long periods in the harsh intracluster environment. For example, heat conduction must be highly suppressed between these galaxies and the surrounding ICM. For these coronae to be common (i.e. long lasting) they must contain a heat source able to combat the radiative energy loss due to the emission of the observed X-rays.

The two dominant galaxies in Coma, NGC 4889 and NGC 4874, show a large line-of-sight velocity difference, $\sim 700 \text{ km s}^{-1}$, between them (Fitchett & Webster 1987). The presence of these galaxies is likely due to a recent cluster merger. The X-ray emission shows that the cluster is in an unrelaxed state (Briel, Henry & Boehringer 1992). One or both of the central galaxies can-

not be at rest in the cluster potential or ICM. Both of the galaxies are associated with galaxy subgroups (Adami et al. 2005).

Here we examine new deep *Chandra* observations of the two galaxies. These observations represent some of the deepest observations by *Chandra* of coronae embedded in clusters. We leave examination of the other coronae in Coma to a later work. The Coma cluster lies at a redshift of 0.0231 (Struble & Rood 1999), implying 1 arcsec on the sky corresponds to 0.47 kpc if $H_0 = 70 \text{ km s}^{-1} \text{ Mpc}^{-1}$.

2 DATA ANALYSIS

We processed the *Chandra* Coma datasets as detailed in Sanders et al. (2013). The total exposure time of the observations is 546 ks (see Table 1). The event files were reprocessed to take advantage of VFAINT grading, if appropriate, and reprojected to the coordinate system of the 13994 observation. No periods from the observations were removed as no flares were observed. Blank-sky-background observations were used to create background event files, adjusting their exposure time to match the 9 to 12 keV count rate in the observed data. Images, background images and exposure maps were created for each observation and combined.

Table 1. *Chandra* datasets examined here. Listed are the observation identifier, date of observation, ACIS detector mode and exposure.

Observation	Date	Mode	Exposure (ks)
555	1999-11-04	FAINT	8.7
1112	1999-11-04	FAINT	9.7
1113	1999-11-04	FAINT	9.6
1114	1999-11-04	FAINT	9.0
9714	2008-03-20	VFAINT	29.6
13993	2012-03-21	VFAINT	39.6
13994	2012-03-19	VFAINT	82.0
13995	2012-03-14	VFAINT	63.0
13996	2012-03-27	VFAINT	123.1
14406	2012-03-15	VFAINT	24.8
14410	2012-03-22	VFAINT	78.5
14411	2012-03-20	VFAINT	33.6
14415	2012-04-13	VFAINT	34.5

2.1 Images

In Fig. 1 we present X-ray images of the two central galaxies, showing the exposure-corrected surface brightness in the 0.5 to 3 keV band (chosen to reduce the projected cluster emission). For the exposure map creation, we assumed a spectral model appropriate for the cluster emission (9.7 keV temperature, $0.24 Z_{\odot}$ metallicity) rather than that for the galactic emission, as the cluster background emission covers a larger spatial region than the galactic emission. The inner peak of X-ray emission is contained within the inner 3.5 arcsec radius for both galaxies.

NGC 4874 hosts a well known wide-angle-tail (WAT) radio source (O'Dea & Owen 1985). Fig. 2 shows an overlay of the radio structure on the X-ray and optical images. The jets of the source appear to be only visible outside the region where the bulk of the X-ray emission originates in the corona. This anti-correlation was first pointed out in NGC 4874 by Sun et al. (2005) using lower resolution radio data. It is outside the corona that the jets will experience any transverse force due to the relative motion of the galaxy and ICM.

2.2 Surface brightness profiles

In Fig. 3 (top panel) we show surface brightness profiles of the two galaxies. The X-ray centroid was used as the centre of the profiles. The profiles were extracted using annuli which were 0.492 arcsec wide and then were rebinned in radius to have a minimum signal to noise ratio of 5. Exposure-corrected background count rates were measured from 49 to 59 arcsec radius (Fig. 4) and subtracted. We excluded point sources identified in Sanders et al. (2013). To show the effect of the PSF, we include on the plot profiles of simulated point sources at the positions of the galaxies. We simulated the point sources for each separate observation using CHART and MARX 5.0.0 (Carter et al. 2003), assuming that they have the same spectrum as their respective galaxy, but ten times the flux. The profiles shown are the combined set of simulations, each reprojected to the 13994 simulation, in the 0.5 to 3 keV energy band.

Both of the central galaxies are more extended than expected for point sources at their locations. Although the PSF at the location of NGC 4889 is larger, this does not account for the noticeably flat X-ray surface brightness profile in its centre, also seen in Fig. 1. The outer parts of the galaxy have a very similar surface brightness profile. The centres of the X-ray emission are consistent within around 0.5 arcsec with the positions of the galaxies.

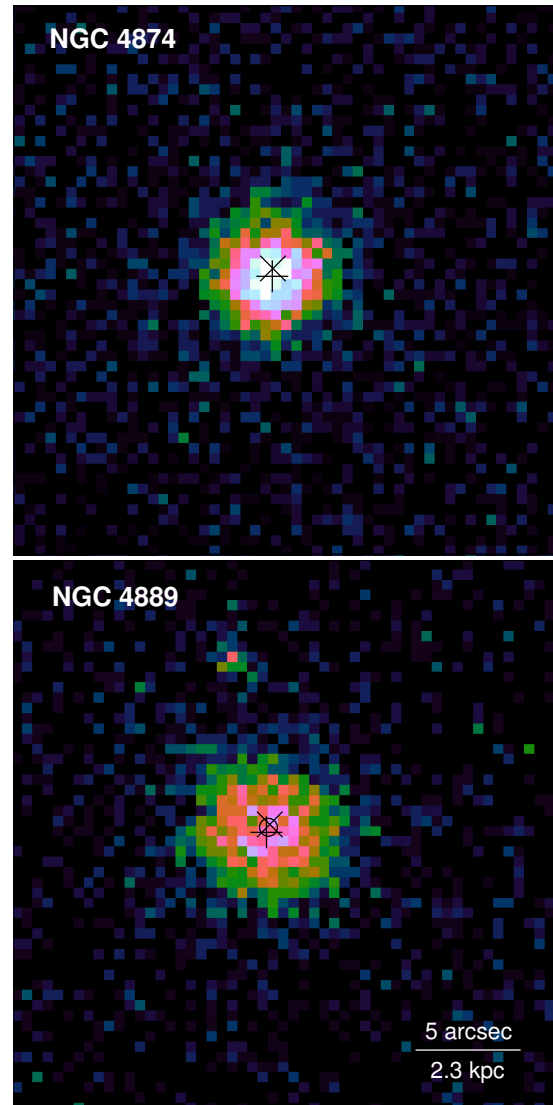


Figure 1. Exposure-corrected X-ray images of the two central galaxies in the 0.5 to 3 keV band. We use native 0.492 arcsec pixels. The images use the same surface brightness colour scale. The marker \times shows the position of the galaxy (NGC 4874 was taken from SDSS; NGC 4889 was taken from the 1.4 GHz radio source position in Miller, Hornschemeier & Mobasher 2009). The marker $+$ shows the X-ray centroid for the inner 4.5 arcsec radius. The centroids of NGC 4874 and NGC 4889 are $12^{\text{h}}59^{\text{m}}35\overset{\text{s}}{.}71$, $+27^{\circ}57'33\overset{\text{s}}{.}0$ and $13^{\text{h}}00^{\text{m}}08\overset{\text{s}}{.}14$, $+27^{\circ}58'36\overset{\text{s}}{.}8$, respectively. Marked by \circ , the 4.9 GHz radio source in NGC 4889 is located at $13^{\text{h}}00^{\text{m}}08\overset{\text{s}}{.}14$, $+27^{\circ}58'37\overset{\text{s}}{.}1$ in the VLA image archive. The positions are consistent within their uncertainties.

The outer X-ray surface brightness profiles are likely to have a significant component from low-mass X-ray binaries (LMXB). This can be modelled by taking the optical profile and assuming a constant ratio between the optical luminosity of the galaxy and its LMXB X-ray emission. Sarazin, Irwin & Bregman (2001) examined NGC 4697, finding a ratio between the LMXB X-ray luminosity in the 0.3 to 10 keV band and B band optical luminosity of $8.1 \times 10^{29} \text{ erg s}^{-1} L_{B\odot}^{-1}$. Kim et al. (2009) examined three old elliptical galaxies, finding a factor of two variation in the ratio between the 0.3 to 8 keV LMXB X-ray luminosity and the K band lumi-

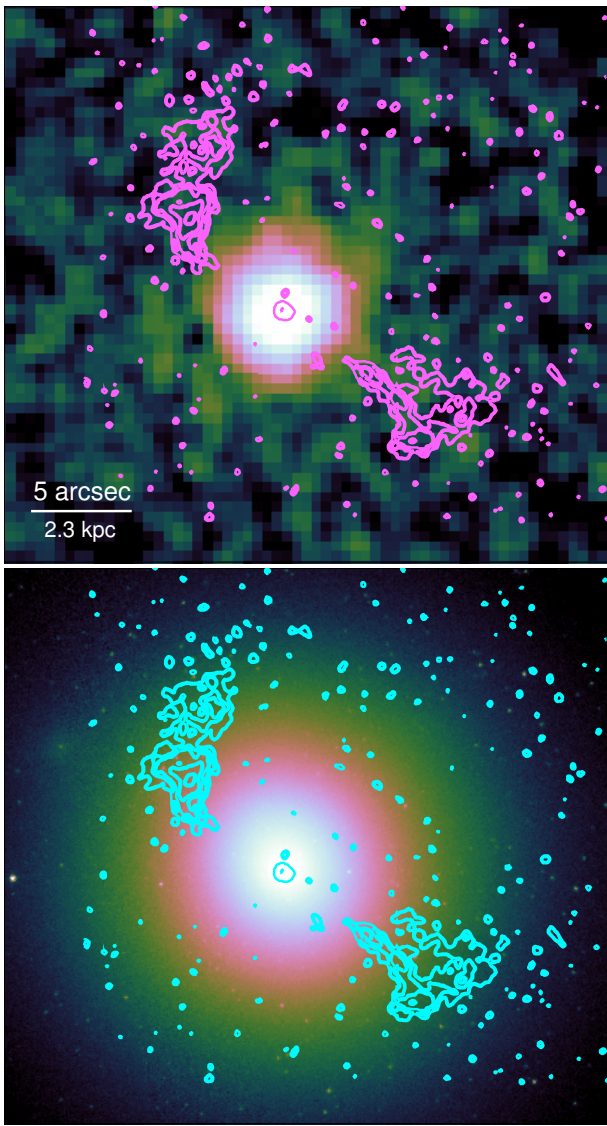


Figure 2. (Top panel) X-ray image of NGC 4874 in the 0.5 to 3 keV band, smoothed with a Gaussian of size 2 pixels. The contours are 6 cm radio data taken from Feretti & Giovannini (1987). (Bottom panel) *HST* F814W ACS image of the galaxy with the same contours.

nosity of $1 - 2 \times 10^{29} \text{ erg s}^{-1} L_{K\odot}^{-1}$, apparently increasing with the globular cluster specific frequency. We show in Fig. 3 the expected surface brightness profiles for the LMXB X-ray contribution. This was calculated by taking the magnitudes of the galaxies (from Sun et al. 2007) and converting to a total X-ray count rates using the different ratios. We assumed a powerlaw LMXB spectrum with $\Gamma = 1.56$ (Irwin, Athey & Bregman 2003). *Hubble Space Telescope* surface brightness profile were made for each galaxy (using filter F814W) and scaled to create X-ray profiles, using the integrated optical light (calculated by fitting a Sérsic profile to the outer parts and adding the inner contribution). Fig. 3 shows the spread in X-ray surface brightness from the different ratios. LMXB are likely to be important in the outskirts of the galaxies, but the exact contribution is difficult to estimate. In addition, we have removed point sources from the data which may be part of this LMXB contribution.

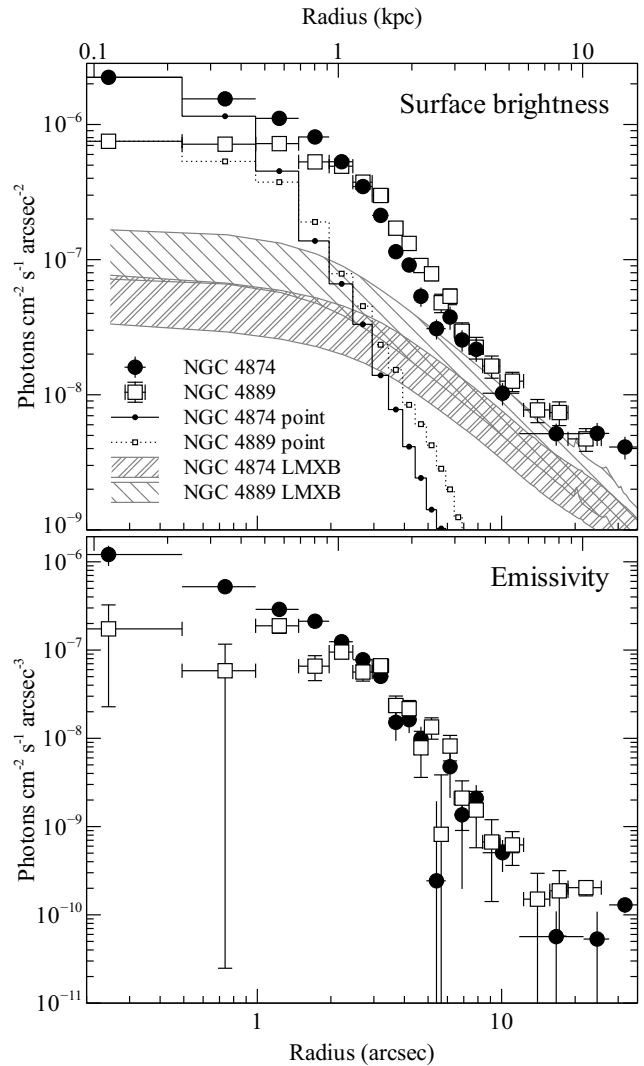


Figure 3. (Top panel) Background-subtracted X-ray surface brightness profile of the two galaxies in the 0.5 to 3 keV band. The two lines labelled ‘point’ are surface brightness profiles for two point sources at the location of the galaxies. We use the X-ray spectrum of the respective galaxy and normalise the profiles to the central values of their respective galaxies. The regions labelled ‘LMXB’ show the expected range of flux from X-ray binaries in the galaxies. (Bottom panel) X-ray emissivity profiles, created by deprojecting the surface brightness profiles.

However, the shape of the measured surface brightness profiles in the outskirts is also dependent on the region used to extract a background surface brightness. Fig. 4 (bottom row) shows that the faint X-ray emission around each galaxy has a complex morphology. It is not obvious what part of that emission is associated with the galaxy and what part with the cluster. If this extended emission has a strong LMXB contribution, then the LMXB emission is not strongly correlated with the optical morphology of the galaxies.

If the WAT source shape indicates the path of NGC 4874 through the cluster, it is heading in a south-east direction (Feretti & Giovannini 1987). Any material stripped from the corona should appear behind the path of the galaxy. We do not see any evidence for excess X-ray emission (Figs. 2 and 4) from such stripped material.

Fig. 3 (bottom panel) shows the 3D radial emissivity, which

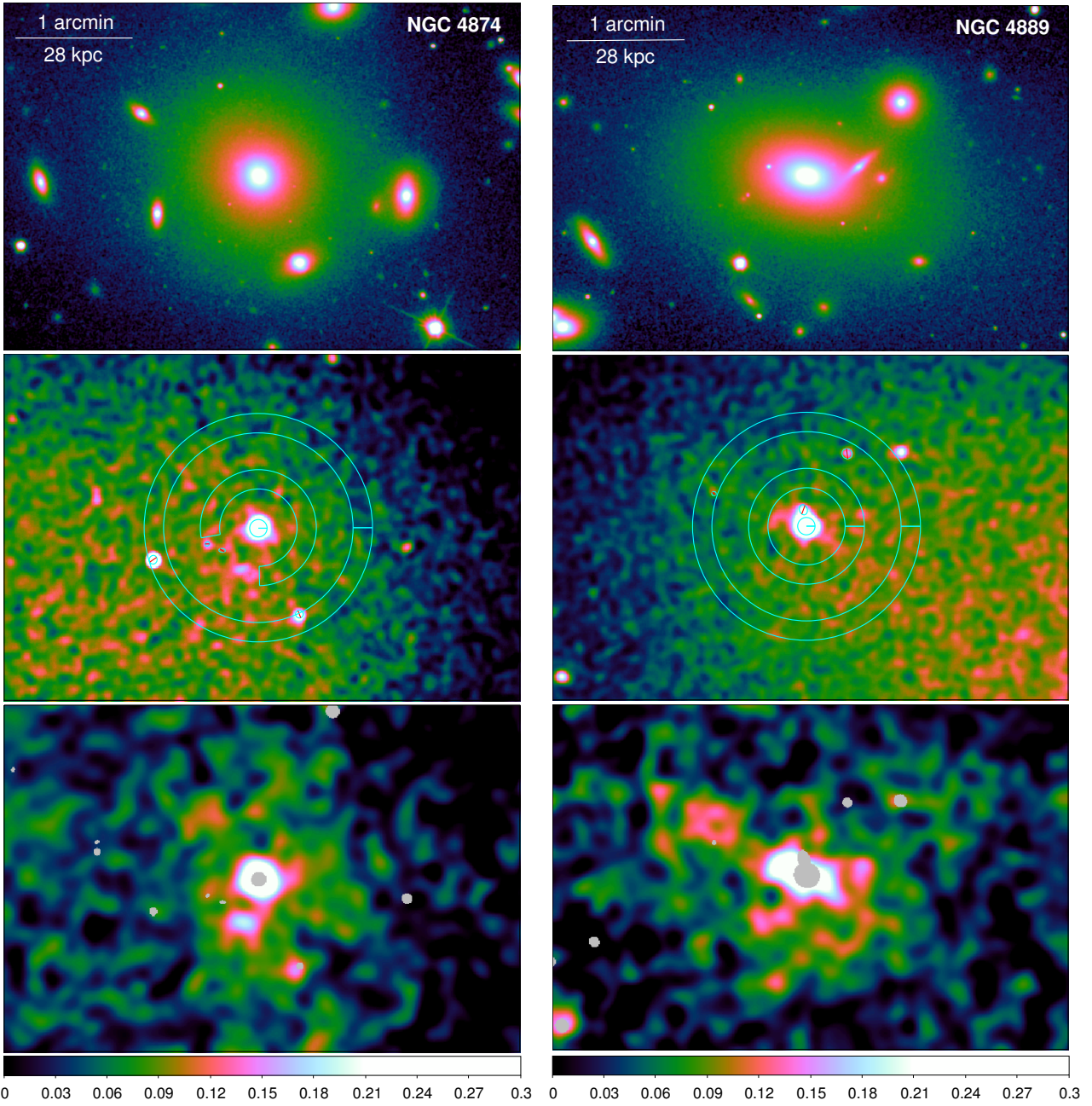


Figure 4. Optical and X-ray images of the outer parts of NGC 4874 (left) and NGC 4889 (right). (Top row) SDSS r band image. (Centre row) 0.5 to 7 keV exposure-corrected-X-ray image of the same region, smooth by a Gaussian with $\sigma = 1.968$ arcsec. Shown are the surface-brightness-background region (outer annulus), spectral background region (inner annulus), galaxy spectral region (circle) and excluded point source (slashed ellipses). (Bottom row) Unsharp-masked image of the same region with point sources, taken from Sanders et al. (2013), excluded (in grey). This shows the fractional difference between the X-ray image smoothed by a Gaussian with $\sigma = 3.94$ and 63.0 arcsec, with the numerical value shown in the colour bars.

is deprojected from the surface brightness under the assumption of spherical symmetry. The emissivity error bars are generated by repeating the deprojection with different input profiles, by making different realisations based on the mean value and the size of the error bars, and examining the distribution of output profiles. For NGC 4889 the emissivity within a radius of 0.2 kpc suddenly drops. The region may be surrounded by a rim of high emissivity (the third innermost radial bin).

2.3 Image fitting

We can examine this hole in more detail including the effect of the PSF. We used SHERPA (Freeman, Doe & Siemiginowska 2001) to fit the X-ray count image in a 64×64 pixel box around NGC 4889. We implemented a density model where the density was zero inside r_{cavity} and a standard β model outside that to some maximum radius (r_{max}). This was then projected onto the sky to make a surface brightness image. The model was fitted to the data by minimis-

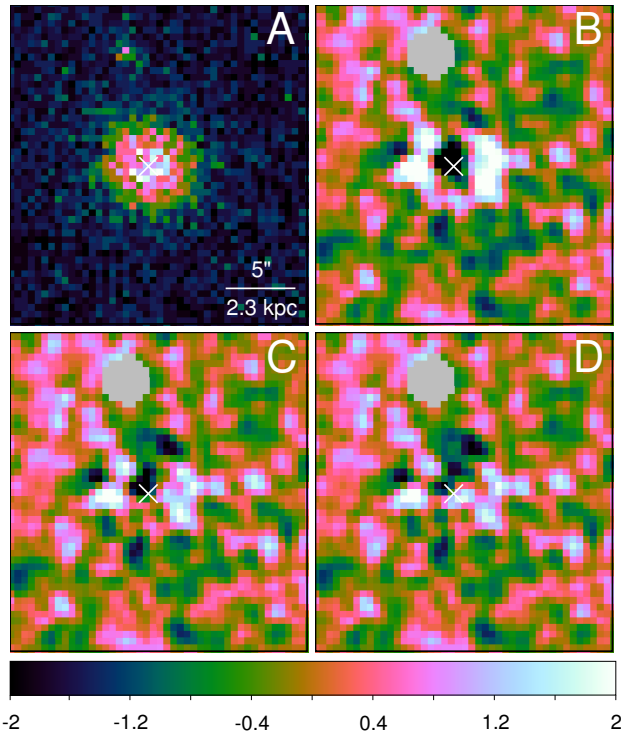


Figure 5. Residuals of surface brightness fits to the NGC 4889 region, accounting for PSF. The point source to the north (grey) is excluded. (A) Original X-ray image (using a different colour scaling), (B) residuals from a β model with fixed $\beta = 2/3$, (C) residuals from a β model with free β parameter and (D) residuals from a β model with a central cavity. The residual images have been smoothed by a Gaussian with $\sigma = 1$ pixel (0.492 arcsec). The colour bar shows the numerical value in counts per pixel.

Table 2. Parameters from β model fits to images.

Object	Parameter	Fixed β	Variable β	Inner cavity
NGC 4889	β	2/3	$1.5^{+0.5}_{-0.3}$	$1.1^{+0.1}_{-0.2}$
	r_{\max} (arcsec)	> 19	> 10	> 10
	r_{cavity} (arcsec)	-	-	$1.2^{+0.2}_{-0.1}$
NGC 4874	β	2/3	0.80 ± 0.06	0.79 ± 0.05
	r_{\max} (arcsec)	> 13	> 12	> 13
	r_{cavity} (arcsec)	-	-	< 0.5

ing the C-statistic, after convolution by the PSF generated using the CHART and MARX simulations. Fig. 5 shows the residuals from the data for three variations of the model, (B) fixing $\beta = 2/3$ with $r_{\text{cavity}} = 0$, (C) a free β parameter with $r_{\text{cavity}} = 0$ and (D) allowing β and r_{cavity} to vary. The final model (D) improved the fit statistic by 10.9 over model (C). Model (D) implies a $r_{\text{cavity}} = 0.6$ kpc.

If the corona of the galaxy is not spherical in shape, it is possible that we could erroneously infer the presence of a cavity. For this to be the case, the corona would have to be a disc lying in the plane of the sky. Any projected emission in front or behind the core should increase the surface brightness. Its morphology should be spherical, unless it is significantly affected by ram pressure.

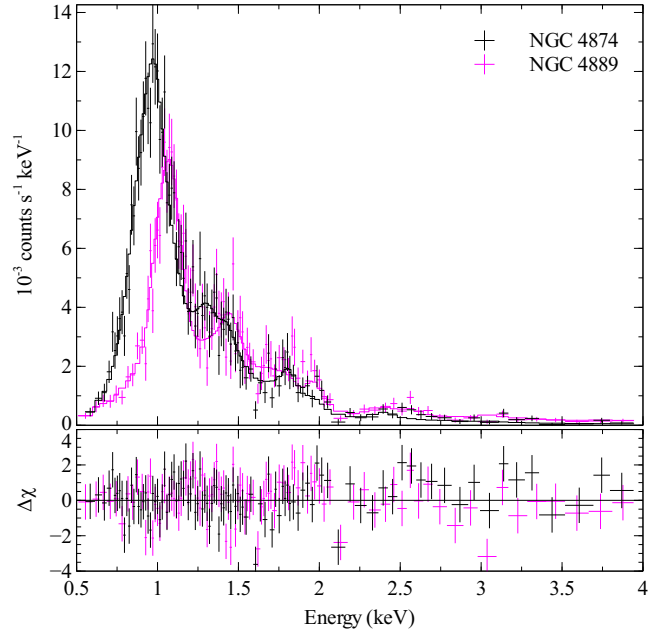


Figure 6. Spectral fit to the background-subtracted X-ray spectra of the galaxies. In these fits the Galactic column density was allowed to be free. Source spectra were extracted from regions 4.5 arcsec in radius. Background spectra were extracted from an annular region 20 to 30 arcsec radius. For NGC 4874 an angular range starting 10 degrees south from the eastern direction and ending in the south direction, was excluded to avoid some point sources (Fig. 4).

2.4 Spectral fitting

Fig. 6 shows fits to the spectra extracted from the two galaxies, after subtraction of the background cluster emission. They were fit between 0.5 and 4 keV using an APEC emission model (Smith et al. 2001), version 2.0.1, with PHABS photoelectric absorption to account for Galactic absorption (Balucinska-Church & McCammon 1992). To analyse the data we used CIAO version 4.5 and CALDB version 4.5.9, which includes recent corrections for the optical blocking filter (OBF) contamination. When creating response matrices and ancillary response matrices, we weighted spatial regions by the number of counts in the 0.5 to 7 keV band. The spectra and background spectra were added together. The response matrices and ancillary response matrices were weighted by the relative exposure times.

The parameters obtained from the spectral fits are shown in Table 3. The first set of spectral fits allow the Galactic column density (n_{H}) to be free. The values from the fits are significantly higher than the value inferred from HI measurements ($0.85 \times 10^{20} \text{ cm}^{-2}$; Kalberla et al. 2005). The best fitting n_{H} values are also unaffected by changing between the contaminant model in CALDB version 4.5.9 and previous versions. The likely explanation is that there are significant problems with the instrumental gain calibration during these Coma observations. If event energies are artificially increased, this can appear to be an increase in absorbing column density. Fig. 7 compares the spectra of the instrumental lines at high energy in the observations taken in 2012, showing that the energy calibration at these energies is not stable. The cause for this gain variation appears to be large changes in the focal plane temperature during the observations (Fig. 8). In particular, observation 13996 spends long periods away from the nominal temperature at which the instrument is calibrated.

Table 3. Spectral fit parameters for the two galaxies. We show the parameters allowing the Galactic column density to be free in the fit, or fixing it at the value of $0.85 \times 10^{20} \text{ cm}^{-2}$ from Kalberla et al. (2005). The data were fit between 0.5 and 4 keV, minimising the χ^2 statistic. We also show the results where the spectra were jointly fit with the background spectra, fitting the data between 0.5 and 7 keV (1T). In this case an APEC model was fit to the corona and background simultaneously, scaling by the areas on the sky and with an additional component for the coronal emission. We list the temperature and metallicity of the background component as ‘‘Background’’. For NGC 4874, we also use a model with a second coronal temperature component, with the metallicity tied to the first component (2T). The flux shown is between 0.5 and 4 keV. The luminosity is bolometric, with absorption removed. The number of counts is between 0.5 and 4 keV after subtracting the projected cluster emission (around 20 per cent of the counts).

Object	Parameter	Fit n_{H}	Fix n_{H}	Joint fit (1T)	Joint fit (2T)
NGC 4874	n_{H} (10^{20} cm^{-2})	15_{-4}^{+5}	0.85	4.4 ± 0.6	4.5 ± 0.7
	kT_1 (keV)	1.04 ± 0.02	1.18 ± 0.02	1.14 ± 0.3	1.04 ± 0.02
	kT_2 (keV)				2.2 ± 0.3
	Z (Z_{\odot})	$0.40_{-0.06}^{+0.09}$	0.40 ± 0.06	0.37 ± 0.06	$1.3_{-0.4}^{+0.6}$
	norm ₁ (10^{-5} cm^{-5})	5.3 ± 0.5	4.2 ± 0.4	4.6 ± 0.4	$1.1_{-0.3}^{+0.4}$
	norm ₂ (10^{-5} cm^{-5})				1.2 ± 0.2
	Background kT (keV)			7.7 ± 0.4	7.5 ± 0.4
	Background Z (Z_{\odot})			0.23 ± 0.06	0.22 ± 0.06
	χ^2_{ν}	$117/98 = 1.19$	$133/99 = 1.34$	$492/426 = 1.15$	$470/424 = 1.11$
	Flux ($10^{-14} \text{ erg cm}^{-2} \text{ s}^{-1}$)	4.2	4.4	4.3	4.4
	Luminosity ($10^{40} \text{ erg s}^{-1}$)	12	9.0	9.9	9.1
	Counts	3335			
NGC 4889	n_{H} (10^{20} cm^{-2})	9 ± 3	0.85	6.3 ± 0.7	
	kT (keV)	1.9 ± 0.1	2.1 ± 0.4	2.0 ± 0.06	
	Z (Z_{\odot})	1.5 ± 0.4	$2.2_{-0.4}^{+0.5}$	1.7 ± 0.3	
	norm (10^{-5} cm^{-5})	3.0 ± 0.5	2.2 ± 0.3	2.8 ± 0.3	
	Background kT (keV)			6.8 ± 0.3	
	Background Z (Z_{\odot})			0.28 ± 0.06	
	χ^2_{ν}	$123/93 = 1.32$	$136/94 = 1.45$	$467/427 = 1.10$	
	Flux ($10^{-14} \text{ erg cm}^{-2} \text{ s}^{-1}$)	3.9	4.0	4.0	
	Luminosity ($10^{40} \text{ erg s}^{-1}$)	9.1	7.9	8.8	
	Counts	3768			

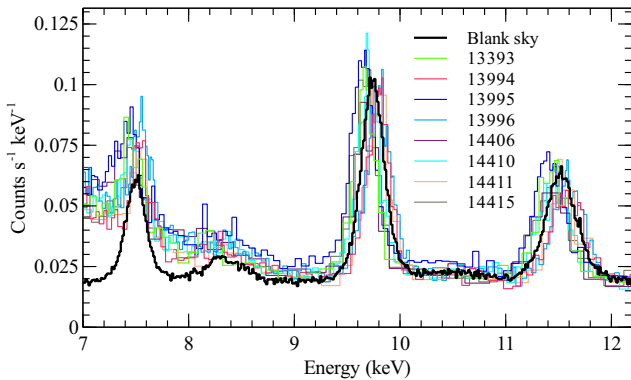


Figure 7. Comparison of the spectra of the instrumental lines in the observations taken in 2012 for the ACIS-I2 CCD. Also plotted is a spectrum taken from blank sky observations, appropriate for the time period. The spectra have been rebinned to have a signal to noise of 10 per spectral bin.

Unfortunately, these gain changes cannot easily be compensated for in the analysis. We attempted to find the gain variation by jointly fitting the spectra of the surrounding cluster emission (0.4 to 1.4 arcmin radius) from each of the observations. The gain was allowed to vary using the gain fit feature in XSPEC with the column density fixed to the HI value. If these gain corrections were then applied to the spectra of the galaxies, they did not appear to significantly reduce the best fitting column density. This lack of improvement could be because the gain variations are not simple linear shifts. In addition, residual spectral features not adequately fit by the spectral model may affect the best fitting gain values.

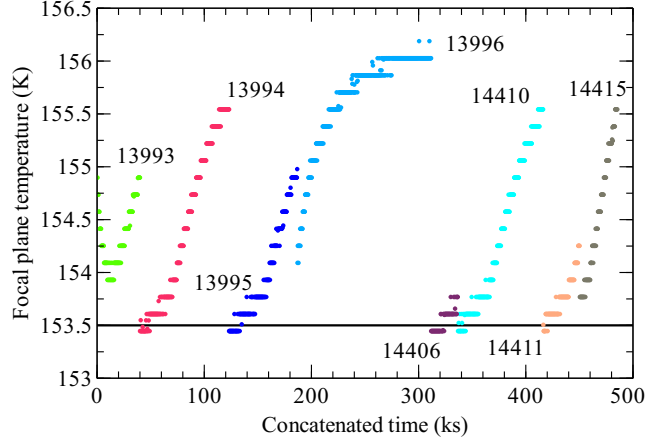


Figure 8. Focal plane temperature during the 2012 observations. The observation times are relative to the end of the time of previous observation identifier. The horizontal line shows the ACIS nominal temperature.

We therefore caution that the spectral parameters we derive are subject to systematic uncertainties. When fitting for gain variations and applying them to the combined spectra of the corona, we obtained for NGC 4889 changes in temperature of around 0.2 keV, abundance $0.2 Z_{\odot}$ and 20 per cent normalisation. The likely systematic uncertainties from the gain calibration are likely of this order. If the spectra from each observation were jointly fit for NGC 4889, allowing for different gain shifts in each, smaller changes than this were found.

As the surrounding background regions are similarly affected by gain issues, to investigate the systematics further, we jointly fit the background cluster spectra (using the regions shown in Fig. 4) and the spectra of coronae. The fits used a common APEC component to account for the cluster emission and another component for the coronal emission. Both components were absorbed by a common absorption model. The resulting spectral parameters (Table 3), except for n_{H} , are similar to the previous fits where the background was subtracted from the coronal spectra. We also investigated the use of earlier versions of the APEC spectral model which has significantly different models for the Fe-L spectral lines. If version 1.3.1 is used instead of 2.0.1, the best fitting temperatures change slightly to 0.99 and 1.79 keV for NGC 4874 and 4889, respectively, when fitting for n_{H} .

The spectrum of NGC 4874 allows the inclusion of a second thermal component with a temperature of around 2 keV. The addition of this component significantly reduces the χ^2 of the fit and raises the best fitting metallicity to $1.3 Z_{\odot}$ (assuming both coronal components have the same metallicity). The hotter second component is likely due to material at larger radius in the corona. If a smaller extraction and background region are used, the hotter component reduces in significance. A second component added to the NGC 4889 spectral fit cannot have its temperature constrained.

To examine the properties of the coronae as a function of radius we examined spectra extracted from annular regions. In Fig. 9 we plot the spectral profiles of the density and temperature for the two galaxies. The temperatures shown were obtained by fitting the projected spectra and deprojected spectra calculated using the DS-DEPROJ algorithm (Sanders & Fabian 2007; Russell, Sanders & Fabian 2008). The spectra were fit with an APEC thermal model, fixing the metallicity and absorbing Hydrogen column density to the best fitting single component value (Table 3). The profiles show that the effect of projection in these spectra is relatively small. As was found by Vikhlinin et al. (2001), the temperature in NGC 4874 rises with radius in the inner few arcsec. In NGC 4889, there may be a mild rise in temperature with radius. The temperatures rapidly rise at a radius of 2.5 to 5 kpc, where the surface brightness is rapidly declining. We note, however, that in both galaxies there may be a significant contribution to the spectra from LMXB emission in the outer parts. The density profile for NGC 4889, like the emissivity, shows a depression in density in the central region.

We looked for non-thermal powerlaw emission from the nuclei of the two galaxies. We examined the emission inside 1.5 arcsec radius from the X-ray centroid for the two galaxies, using the a region of 1.5 to 2.5 arcsec as a background region. A model comprising of an APEC component plus a powerlaw with its photon index fixed to 1.7 was fitted to the spectra. We used a range of fixed values for the absorption and metallicity, taken from Table 3. We obtained upper limits for 2–10 keV X-ray luminosity for NGC 4874 and 4889 of 1×10^{39} and 3×10^{39} erg s $^{-1}$, respectively, at the 90 per cent confidence level. Using a smaller extraction region for NGC 4889 (1 arcsec, with 1 to 2 arcsec background) gives an improved limit of 1×10^{39} erg s $^{-1}$.

The metallicity from the single temperature component fit of NGC 4874 appears to be significantly lower than for NGC 4889 (0.37 compared to $1.5 Z_{\odot}$, respectively). However, if a second thermal component is included in the NGC 4874 spectral fit, its metallicity increases to be consistent with NGC 4889. The measurement of metalicities at ~ 1 keV temperatures is difficult due to the weak continuum relative to the line emission. Examining the residuals of the single temperature component model to the NGC 4874 data shows an excess emission above 4 keV. This is likely due to the

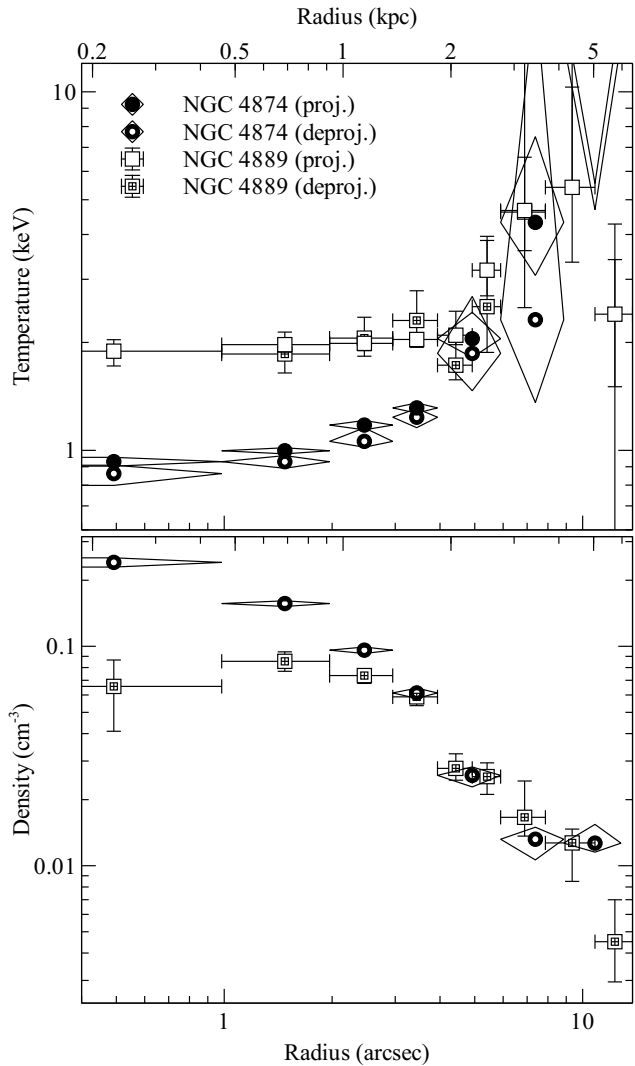


Figure 9. (Top panel) Temperature profiles for the galaxies, fitting projected and deprojected spectra. (Bottom panel) Electron density profiles, calculated from the normalisations of the deprojected spectral fits. Note that these fits do not include the spectral contribution from LMXB emission. The deprojected temperature of the innermost annulus of NGC 4889 could not be constrained, so the density is calculated assuming the projected temperature.

temperature gradient within the corona or it could be due to an increasing contribution of LMXB powerlaw emission with radius. We note that previously Vikhlinin et al. (2001) obtained a metallicity for NGC 4874 of $0.79^{+0.84}_{-0.22}$ using a single component, which is greater than our single component fit result. It is possible that this difference may be due to the gain calibration uncertainties. We verified that the choice of MEKAL or APEC did not significantly change the results of the spectral fits. The background region used by Vikhlinin et al. (2001) (15 to 30 arcsec radius) is similar to the one used here (20 to 30 arcsec radius), so this is unlikely to cause the metallicity difference.

We can also attempt to determine the metallicities of the coronae relative to Fe to examine enrichment scenarios. However, the results depend on the spectral code used. For NGC 4874, we fit the background-subtracted spectrum between 0.5 and 7 keV, forcing the column density to the value from fitting the cluster material and

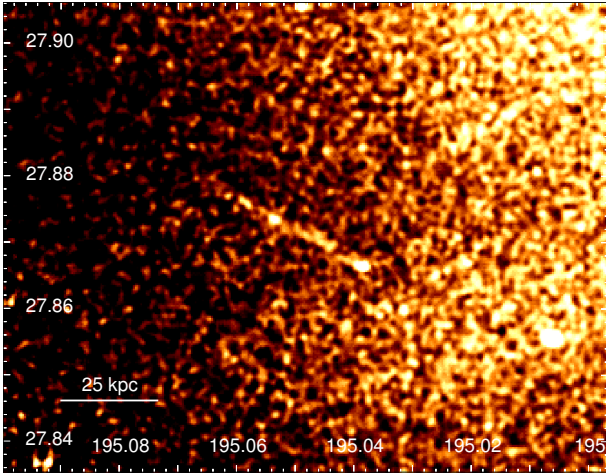


Figure 10. 0.5 to 1.5 keV X-ray image of the tail behind galaxy D100 / GMP 2910. The image was binned into 0.984 arcsec pixels and smoothed by 3 pixels.

allowing the α -elements to vary in their solar proportions relative to iron, with the other elements fixed to have the same ratio to solar as iron, we obtain a relative ratio of α to Fe of $1.3 \pm 0.2 Z_{\odot}/Z_{\odot}$, using the APEC model. However, if Ni is allowed to vary, the peak emission in the Fe-L region is instead fit by a very high Ni to Fe ratio (~ 13), changing the α to Fe ratio to 2.3. Using the CIE model from SPEX (Kaastra, Mewe & Nieuwenhuijzen 1996) gives an α to Fe ratio of 1.1 ± 0.2 , if Ni is fixed to Fe, or 1.4 ± 0.2 , if Ni is allowed to vary (giving a Ni to Fe ratio of $5.0^{+2.1}_{-1.4}$). For NGC 4889, we obtain similar results where the α to Fe ratios are 1.2 ± 0.2 and 1.0 ± 0.2 , for APEC and SPEX, respectively, if Ni is tied to Fe. If Ni is free to vary, the ratios change to $1.9^{+0.6}_{-0.4}$ and 1.1 ± 0.2 , respectively. We note that the implemented ionization balance for Ni in the current plasma codes is inaccurate and can significantly bias the Ni abundance measurements. Taking into account this and the gain calibration uncertainties, the metallicity ratios in the coronae appear consistent with Solar values.

2.5 Stripped tail

Yagi et al. (2007) showed the existence of a 60-kpc-long filament of $H\alpha$ emission behind the galaxy GMP 2910 (also known as D100). As discussed in Sanders et al. (2013), there is soft X-ray emission associated with the filament (Fig. 10). The extent and location of the tail appears to be the same as the $H\alpha$ emission (50 kpc), except for the faintest structure at the end furthest from the galaxy. The filament appears to be ~ 7 arcsec wide or around 3 kpc.

To examine the spectrum of the tail we fit a joint model to the tail and the surrounding projected emission (Fig. 11). The spectra were fit simultaneously between 0.5 and 4 keV, minimising the C-statistic. The emission from the tail was assumed to be the cluster emission (scaled by area) plus its own thermal component. In the fits the absorbing column density was free, but linked between the two components.

Using a single component APEC for the tail, its temperature is 1.0 ± 0.1 keV assuming its metallicity is $0.3 Z_{\odot}$. The best fitting value of n_H is $(1.5 \pm 0.9) \times 10^{20} \text{ cm}^{-2}$. The bolometric luminosity of the tail is $1 \times 10^{40} \text{ erg s}^{-1}$ and the spectrum has 538 net counts above the cluster background in the 0.5 to 7 keV band. The 0.5 to 2 keV flux is $6 \times 10^{-15} \text{ erg cm}^{-2} \text{ s}^{-1}$. If the metallicity is allowed to

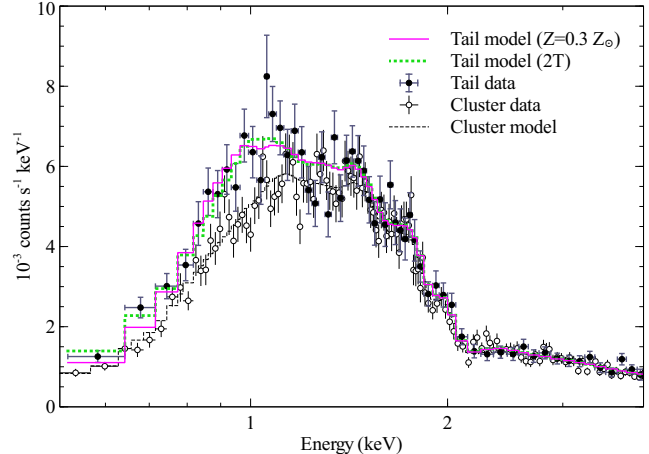


Figure 11. Spectrum in the tail region compared to the nearby cluster spectrum. The cluster spectrum has been scaled to the same area as the tail and both have been rebinned for display to have a minimum signal to noise ratio of 8. Shown are models for the cluster emission and the cluster plus tail model spectrum assuming $0.3 Z_{\odot}$ metallicity for the tail. We also show a model where a second thermal component was fit to the tail (2T).

vary, its best fitting value is rather low at $0.09^{+0.13}_{-0.06} Z_{\odot}$, which gives a lower 0.9 ± 0.1 keV temperature.

A second thermal APEC component can be included in the spectral fit for the tail, assuming both components have the same metallicity. In this case, the two temperatures obtained are $0.21^{+0.07}_{-0.04}$ and $1.3^{+0.4}_{-0.3}$ keV and n_H is $(2.3 \pm 0.9) \times 10^{20} \text{ cm}^{-2}$. The C-Statistic for the spectral fit reduces from 317 to 311 (changing from 365 to 362 degrees of freedom). With the second component, the best fitting metallicity is $0.6^{+1.9}_{-0.5} Z_{\odot}$. The bolometric luminosity in this case increases to $4 \times 10^{40} \text{ erg s}^{-1}$ and the flux is $9 \times 10^{-15} \text{ erg cm}^{-2} \text{ s}^{-1}$. Similar low temperature single-component metallicities and second temperature components have been seen in spectra from other stripped tails (e.g. Zhang et al. 2013). We examined the spectra of the front and back halves of the tail, fitting single thermal components for the tail emission. We found that they have consistent ~ 1 keV temperatures.

Taking the single component model, the electron density of the X-ray emitting material in the tail is $8 \times 10^{-3} \text{ cm}^{-3}$, assuming the emission fills a cylinder 2 kpc in radius and 36 kpc in length. If the material is clumpy, this value would be a lower limit. The density gives a gas mass of $10^8 M_{\odot}$, similar to the amount of material in ionised gas (Yagi et al. 2007). If the metallicity of the material is $0.3 Z_{\odot}$ and its temperature 1 keV, the implied radiative cooling time is 2 Gyr. If the galaxy is travelling around the sound speed relative to the cluster ($\sim 1500 \text{ km s}^{-1}$), it would traverse the length in a tail in around 20 Myr. Therefore radiative cooling is not an important physical process here.

The X-ray emission from the galaxy itself is consistent with a thermal spectrum with a 0.77 ± 0.09 keV temperature. In these fits the absorbing column density and metallicity were free, although the metallicity is poorly constrained and the best fitting column density is zero. The spectrum has 176 counts above the background and the bolometric luminosity of the model is $4.5 \times 10^{39} \text{ erg s}^{-1}$ and the flux is $2 \times 10^{-15} \text{ erg cm}^{-2} \text{ s}^{-1}$.

3 DISCUSSION

3.1 Central cavity or cavities

In clusters of galaxies, cavities are routinely observed in the intracluster medium (for reviews see McNamara & Nulsen 2007 and Fabian 2012). These cavities are inflated by jets, filled with bubbles of relativistic plasma and are likely to combat cooling as they do work on their surroundings. In the coronae of galaxies, radio jets are found to be anti-correlated with the X-ray emission, as seen in several objects besides NGC 4874, e.g. NGC 1265 (Sun, Jerius & Jones 2005) and ESO 137-006 (Jones & McAdam 1996). In NGC 1265 there are small X-ray indentations east and west of the nucleus where the jets leave the coronal gas.

The best fitting model for the density distribution in NGC 4889 has a cavity or no X-ray emission inside 0.6 kpc radius. The residuals in Fig. 5 do not obviously show the presence of two cavities, as usually found in clusters. These features are usually found in pairs, similarly to the radio jets they are created by. In NGC 4889 the cavities, if present, are likely aligned along the line of sight. An alternative possibility is that instead of X-ray cavities, the central X-ray depression is due to a shock generated from an outburst (e.g. Heinz, Reynolds & Begelman 1998). However, we do not observe any central temperature increase associated with a shock. If the central cavity (or cavities; from here on we shall refer to a single cavity for simplicity) is filled by relativistic material ($\gamma = 4/3$), its enthalpy is $4PV$, where P is the pressure (here assumed to be the external pressure) and V is its volume. Taking a density of 0.084 cm^{-3} and temperature of 1.82 keV , we estimate that the cavity enthalpy is $5 \times 10^{55} \text{ erg}$.

The timescale for a bubble of radius r takes to rise to a radius R at its buoyancy velocity is $R/(0.5v_K\sqrt{r/R})$ (Churazov et al. 2000), where v_K is the Keplerian velocity. Taking a velocity dispersion of $\sim 380 \text{ km s}^{-1}$ (McConnell et al. 2011), the buoyancy timescale for a 0.3 kpc radius bubble is 1 or 2 Myr, using $R = 0.3$ and 0.6 kpc, respectively. R may be larger than this, although it cannot be so large that it displaces the bubbles away from the central peak in emissivity and reduces the flattening in the surface brightness profile.

Taking the enthalpy and the 2 Myr timescale, the power needed to inflate the cavity would be $8 \times 10^{41} \text{ erg s}^{-1}$. Therefore during the period of activity the central black hole was supplying energy at a rate one order of magnitude greater than that lost by X-ray emission. The scatter in relations of mechanical heating power versus X-ray luminosity are of the order of one order of magnitude (e.g. Bîrzan et al. 2004; Dunn & Fabian 2006) and so this outburst is not too dissimilar to that found in clusters. The enthalpy of the bubble is about an order of magnitude lower than the thermal energy of the corona ($\sim 5 \times 10^{56} \text{ erg}$ within 3 kpc), so the total energy accumulated during current 1-2 Myr long outburst is insufficient to disrupt the corona. The energy in the outburst may also go into lifting the coronal gas in the gravitational potential. $5 \times 10^{55} \text{ erg}$ would lift the corona by $\sim 0.1 \text{ kpc}$, using the gravitational acceleration at 3 kpc radius.

As noted above, in most coronae the radio jets and lobes are anti-correlated with the X-ray gas. This may be due to pressure differentials between the external medium and the relativistic material (Heinz & Churazov 2005). Inside the jets/lobes the pressure will be constant due to the high sound speed. However, in the corona there will be a radial pressure gradient, where the pressure declines with radius and the profile flattens outside in the ICM. There might be an effect similar to what occurs when the end of a toothpaste tube is

squeezed; the radio channel will be closed by the coronal pressure and the relativistic material displaced to larger radius into the ICM.

3.2 Bondi accretion

The black hole in NGC 4889 is one of the most massive known, with a mass around $2 \times 10^{10} M_\odot$ (McConnell et al. 2011). Both NGC 4874 and 4889 show little evidence for dust in the HST F475W data. Additionally, examining the Herschel 70 to 350 micron bands does not show emission which would be associated with significant amounts of cold dust. It is unlikely that any central X-ray surface brightness depression in NGC 4889 could be the result of obscuration. Therefore hot accretion is a plausible fuelling mechanism for the massive black hole in NGC 4889. For such a massive black hole it may be possible to resolve the material close at the Bondi radius. However, if there is a cavity, then much of this material is likely to have been driven out.

The innermost temperature of the corona is around 1.9 keV. The Bondi radius, $r_B = 2GM/c_s^2$, for a black hole of mass M and a sound speed of c_s , would be around 0.3 kpc, close to the cavity radius. The Bondi accretion rate depends on the density at the Bondi radius, which might be zero due to the presence of the cavity. However, if we take the innermost value of the entropy ($\sim 9 \text{ keV cm}^{-2}$) and use the relation in Sun (2009), this implies the Bondi accretion rate is $0.2 M_\odot \text{ yr}^{-1}$. This translates into a heating rate of $10^{45} \text{ erg s}^{-1}$ at 10 per cent efficiency, which is around four orders of magnitude greater than the X-ray luminosity of the galaxy. Inefficient accretion flows have been inferred in other objects, such as the very massive black hole in NGC 1277 (Fabian et al. 2013), Sgr A* at the centre of our galaxy (Rees 1982; Narayan, Yi & Mahadevan 1995) and M87 (Di Matteo et al. 2003). It is possible that the density has been enhanced around the central cavity if material has been swept up by the outburst.

The black hole scaling relation with velocity dispersion suggests a black hole mass for NGC 4874 of $1.7 \times 10^9 M_\odot$ (McConnell & Ma 2013) using $\sigma = 290 \text{ km s}^{-1}$ (Thomas et al. 2007), although scaling relations predict a much smaller black hole mass for NGC 4889 than measured. Similarly, the Bondi accretion rate inferred for NGC 4874 is $0.01 M_\odot \text{ yr}^{-1}$, if the inner entropy is 2.2 keV cm^{-2} . This would translate into an accretion luminosity of $6 \times 10^{43} \text{ erg s}^{-1}$. This is over two orders of magnitude greater than the energy lost by the X-ray emission of the galaxy. In NGC 4874 the cooling rate in the absence of heating should be $\sim 0.3 M_\odot \text{ yr}^{-1}$.

NGC 4889 hosts a point-like radio source with a 5 GHz spectral luminosity of $\sim 10^{28.0} \text{ erg s}^{-1} \text{ Hz}^{-1}$ (Birkinshaw & Davies 1985), coincident with the centre of the galaxy. An extended source at 1.4 GHz was also detected by Miller, Hornschemeier & Mobasher (2009) with $\sim 10^{28.1} \text{ erg s}^{-1} \text{ Hz}^{-1}$. If we use the most likely black hole mass ($2.1 \times 10^{10} M_\odot$), the black hole activity fundamental plane (Merloni, Heinz & di Matteo 2003) suggests that the X-ray luminosity of the nucleus should be $\sim 2 \times 10^{37} \text{ erg s}^{-1}$. This is well below the upper limit ($\sim 10^{39} \text{ erg s}^{-1}$) we obtain in Section 2.4. The inferred mechanical heating power from the radio luminosity (Bîrzan et al. 2008) is around three times smaller than calculated from the cavity enthalpy and timescale. This is well within the large scatter in the mechanical power to radio luminosity relation. High resolution radio observations of NGC 4889 should show high frequency radio emission occupying the cavity at the centre. NGC 4874 has a core flux density at 5 GHz of $\sim 10^{28.1} \text{ erg s}^{-1} \text{ Hz}^{-1}$ (Feretti & Giovannini 1987). Again, the X-ray luminosity of the black hole as estimated from the fun-

damental plane ($6 \times 10^{38} \text{ erg s}^{-1}$) is below the upper limit of $3 \times 10^{39} \text{ erg s}^{-1}$.

It appears that in NGC 4889 that an AGN outburst is displacing the X-ray emitting material in the centre. This is a clear case where the AGN is affecting the corona directly. However, the case of NGC 4874 appears to be the more common among coronal sources. The radio jets, if present, are only visible outside the corona. In this case, the jets appear to have passed their way through the corona before a significant amount of their energy has been dissipated. However, the core radio power of the two galaxies are very similar, which could imply similar accretion rates (Merloni, Heinz & di Matteo 2003).

3.3 NGC 4889 coronal temperature

The temperature of the NGC 4889 corona is the highest known for a galactic coronae (Sun et al. 2007; Sun 2009). However the galaxy does have a high velocity dispersion (McConnell et al. 2011). Sun et al. (2007) compare its temperature with its velocity dispersion (using β_{spec}). Although there are other galaxies with similar temperatures and velocity dispersions, it is the hottest of those. There may be some heating due to the AGN activity in its centre, although it depends on the stage of the outburst. The gravitational potential of the very massive black hole can also affect the gas pressure and temperature if it is in hydrostatic equilibrium. We deprojected the X-ray surface brightness to fit the observed spectral temperature profile assuming hydrostatic equilibrium, fitting for the parameters of an NFW mass model and the outer pressure (the algorithm is detailed in Sanders et al. 2010). If the black hole potential is also included, we find that the contribution to the gas temperature or pressure is only significant in the inner ~ 1.5 arcsec radius. Therefore the mass of the black hole is not a significant direct contributor to the high temperature of the galactic corona.

3.4 Stellar mass loss

The X-ray gas masses for the galaxies within a radius of 3 kpc are $1.2 \times 10^8 M_{\odot}$ and $9.4 \times 10^7 M_{\odot}$, for NGC 4874 and NGC 4889, respectively. If we adopt a value for the stellar mass loss rate of $2.1 \times 10^{-12} M_{\odot} \text{ yr}^{-1} (L_K/L_{K,\odot})^{-1}$, we estimate that the stellar mass loss rate for NGC 4889 is $1.7 M_{\odot} \text{ yr}^{-1}$. Therefore this could replace the material within the X-ray corona in 54 Myr, although the X-ray corona (using a radius of 3 kpc) lies only within the inner 1/3 of the optical light from the galaxy. This could reduce the mass loss rate able to contribute to the corona to $0.6 M_{\odot} \text{ yr}^{-1}$ and the replacement timescale to 0.2 Gyr. However, if the stellar mass loss outside the corona were to form overdense blobs, it might be possible for these to fall towards the centre of the galaxy and contribute to the replacement of the corona. Stellar mass loss may also not mix in a simple way with the coronal material (Panagoulia, Fabian & Sanders 2013). The K band luminosity of NGC 4874 is around 2/3 that of NGC 4889, its coronal gas mass is 30 per cent greater and 1/4 of the optical light is within 3 kpc, so the mass loss rate is around $0.3 M_{\odot} \text{ yr}^{-1}$ and the replacement timescale is 0.4 Gyr.

These resupply timescales can be compared to the mean radiative cooling times in the centre of NGC 4874 and NGC 4889 of 0.04 and 0.2 Gyr, respectively, computed using X-ray surface brightness deprojection, including the black hole mass for NGC 4889. We calculate a mass deposition rate, the cooling rate in the absence of heating, of ~ 0.3 and $0.15 M_{\odot} \text{ yr}^{-1}$ for NGC 4874 and NGC 4889, respectively, within a radius of a few arcsec, including the effect

of the gravitational potential. If the coronae are radiatively cooling, stellar mass loss would be sufficient to replace the material lost by cooling.

In NGC 4889 the kinetic power of stellar mass loss, $(3/2)\dot{M}_{\star}\sigma_{\star}^2 \sim 8 \times 10^{40} \text{ erg s}^{-1}$, is approximately sufficient to replace the energy lost by X-ray emission. In NGC 4874, the lower stellar mass loss rate and velocity dispersion (290 vs 380 km s $^{-1}$), give a kinetic power around five times lower than the X-ray luminosity. Sun et al. (2007) find that in their sample of coronae the stellar mass loss kinetic power is on average a factor of 3.5 times lower than the X-ray luminosity, indicating further sources of heat are required if mass loss from outside the coronal region does not affect the corona.

Both galaxies show the presence of star formation. Using the *WISE* band 4, we obtain star formation rates of $\sim 0.1 - 0.2 M_{\odot} \text{ yr}^{-1}$ using the relation of Lee, Hwang & Ko (2013) with a Kroupa initial mass function. If we combine *GALEX* FUV and *WISE* fluxes, using the relation of Hao et al. (2011), we obtain star formation rates of $\sim 0.3 M_{\odot} \text{ yr}^{-1}$. The inferred star formation rates are close to the $\sim 0.2 M_{\odot} \text{ yr}^{-1}$ cooling rates expected in the absence of heating. If the black hole in NGC 4874 is depositing its energy outside of the corona, it may be ineffective in preventing the cooling taking place. The relatively high star formation rate in NGC 4889 is at odds with the current energy input of the AGN. This could be reconciled if the timescale for the evolution of the bubbles was underestimated or if the AGN input was intermittent.

ACKNOWLEDGEMENTS

We thank A. Vikhlinin for helpful discussions about the gain variation. Support for this work was provided by the National Aeronautics and Space Administration through *Chandra* Award Number GO2-13145X issued by the *Chandra X-ray Observatory* Center, which is operated by the Smithsonian Astrophysical Observatory for and on behalf of the National Aeronautics Space Administration under contract NAS8-03060. The scientific results reported in this article are based on observations made by the *Chandra X-ray Observatory* and data obtained from the *Chandra Data Archive*.

REFERENCES

- Adami C., Biviano A., Durret F., Mazure A., 2005, *A&A*, 443, 17
- Balucinska-Church M., McCammon D., 1992, *ApJ*, 400, 699
- Birkinshaw M., Davies R. L., 1985, *ApJ*, 291, 32
- Birzan L., McNamara B. R., Nulsen P. E. J., Carilli C. L., Wise M. W., 2008, *ApJ*, 686, 859
- Birzan L., Rafferty D. A., McNamara B. R., Wise M. W., Nulsen P. E. J., 2004, *ApJ*, 607, 800
- Briel U. G., Henry J. P., Boehringer H., 1992, *A&A*, 259, L31
- Carter C., Karovska M., Jerius D., Glotfelty K., Beikman S., 2003, in *Astronomical Society of the Pacific Conference Series*, Vol. 295, *Astronomical Data Analysis Software and Systems XII*, Payne H. E., Jedrzejewski R. I., Hook R. N., eds., p. 477
- Churazov E., Forman W., Jones C., Böhringer H., 2000, *A&A*, 356, 788
- Di Matteo T., Allen S. W., Fabian A. C., Wilson A. S., Young A. J., 2003, *ApJ*, 582, 133
- Dunn R. J. H., Fabian A. C., 2006, *MNRAS*, 373, 959
- Fabian A. C., 2012, *ARA&A*, 50, 455

Fabian A. C., Sanders J. S., Haehnelt M., Rees M. J., Miller J. M., 2013, MNRAS, 431, L38

Feretti L., Giovannini G., 1987, A&A, 182, 15

Fitchett M., Webster R., 1987, ApJ, 317, 653

Freeman P., Doe S., Siemiginowska A., 2001, in Society of Photo-Optical Instrumentation Engineers (SPIE) Conference Series, Vol. 4477, Society of Photo-Optical Instrumentation Engineers (SPIE) Conference Series, Starck J.-L., Murtagh F. D., eds., pp. 76–87

Hao C.-N., Kennicutt R. C., Johnson B. D., Calzetti D., Dale D. A., Moustakas J., 2011, ApJ, 741, 124

Heinz S., Churazov E., 2005, ApJ, 634, L141

Heinz S., Reynolds C. S., Begelman M. C., 1998, ApJ, 501, 126

Irwin J. A., Athey A. E., Bregman J. N., 2003, ApJ, 587, 356

Jones P. A., McAdam W. B., 1996, MNRAS, 282, 137

Kaastra J. S., Mewe R., Nieuwenhuijzen H., 1996, in UV and X-ray Spectroscopy of Astrophysical and Laboratory Plasmas, Yamashita K., Watanabe T., eds., pp. 411–414

Kalberla P. M. W., Burton W. B., Hartmann D., Arnal E. M., Bajaja E., Morras R., Pöppel W. G. L., 2005, A&A, 440, 775

Kim D.-W. et al., 2009, ApJ, 703, 829

Lee J. C., Hwang H. S., Ko J., 2013, ApJ, 774, 62

McConnell N. J., Ma C.-P., 2013, ApJ, 764, 184

McConnell N. J., Ma C.-P., Gebhardt K., Wright S. A., Murphy J. D., Lauer T. R., Graham J. R., Richstone D. O., 2011, Nature, 480, 215

McNamara B. R., Nulsen P. E. J., 2007, ARA&A, 45, 117

Merloni A., Heinz S., di Matteo T., 2003, MNRAS, 345, 1057

Miller N. A., Hornschemeier A. E., Mobasher B., 2009, AJ, 137, 4436

Narayan R., Yi I., Mahadevan R., 1995, Nature, 374, 623

O'Dea C. P., Owen F. N., 1985, AJ, 90, 927

Panagoulia E. K., Fabian A. C., Sanders J. S., 2013, MNRAS, 433, 3290

Rees M. J., 1982, in American Institute of Physics Conference Series, Vol. 83, The Galactic Center, Riegler G. R., Blandford R. D., eds., pp. 166–176

Russell H. R., Sanders J. S., Fabian A. C., 2008, MNRAS, 390, 1207

Sanders J. S., Fabian A. C., 2007, MNRAS, 381, 1381

Sanders J. S., Fabian A. C., Churazov E., Schekochihin A. A., Simionescu A., Walker S. A., Werner N., 2013, Science, 341, 1365

Sanders J. S., Fabian A. C., Frank K. A., Peterson J. R., Russell H. R., 2010, MNRAS, 402, 127

Sarazin C. L., Irwin J. A., Bregman J. N., 2001, ApJ, 556, 533

Smith R. K., Brickhouse N. S., Liedahl D. A., Raymond J. C., 2001, ApJ, 556, L91

Struble M. F., Rood H. J., 1999, ApJS, 125, 35

Sun M., 2009, ApJ, 704, 1586

Sun M., Jerius D., Jones C., 2005, ApJ, 633, 165

Sun M., Jones C., Forman W., Vikhlinin A., Donahue M., Voit M., 2007, ApJ, 657, 197

Sun M., Vikhlinin A., Forman W., Jones C., Murray S. S., 2005, ApJ, 619, 169

Thomas J., Saglia R. P., Bender R., Thomas D., Gebhardt K., Magorrian J., Corsini E. M., Wegner G., 2007, MNRAS, 382, 657

Vikhlinin A., Markevitch M., Forman W., Jones C., 2001, ApJ, 555, L87

Yagi M., Komiyama Y., Yoshida M., Furusawa H., Kashikawa N., Koyama Y., Okamura S., 2007, ApJ, 660, 1209

Zhang B. et al., 2013, ApJ, 777, 122